Bioorganic Chemistry 90 (2019) 103018

Contents lists available at ScienceDirect

Bioorganic Chemistry

journal homepage: www.elsevier.com/locate/bioorg

Improving the catalytic efficiency of aldo-keto reductase *Km*AKR towards *t*-butyl 6-cyano-(3*R*,5*R*)-dihydroxyhexanoate via semi-rational design

Han Yu[1], Shuai Qiu[1], Feng Cheng, Ying-Nan Cheng, Ya-Jun Wang*, Yu-Guo Zheng

Key Laboratory of Bioorganic Synthesis of Zhejiang Province, College of Biotechnology and Bioengineering, Zhejiang University of Technology, Hangzhou 310014, PR China

Engineering Research Center of Bioconversion and Biopurification of the Ministry of Education, Zhejiang University of Technology, Hangzhou, Zhejiang 310014, PR China

The National and Local Joint Engineering Research Center for Biomanufacturing of Chiral Chemicals, Zhejiang University of Technology, Hangzhou 310014, PR China

ARTICLE INFO

Keywords:
Aldo-keto reductase
Semi-rational design
t-Butyl 6-cyano-(3*R*,5*R*)-dihydroxyhexanoate
Asymmetric bio-reduction

ABSTRACT

t-Butyl 6-cyano-(3*R*,5*R*)-dihydroxyhexanoate ((3*R*,5*R*)-**2**) is an important chiral diol synthon of atorvastatin calcium. Previously, we constructed a variant *Km*AKR-W297H (M1) of *Kluyveromyces marxianus* aldo-keto reductase (*Km*AKR, designated as M0), possessing excellent diastereoselectivity but moderate activity towards *t*-butyl 6-cyano-(5*R*)-hydroxy-3-oxohexanoate ((5*R*)-**1**). In this work, *Km*AKR-W297H/Y296W/K29H (M3) was developed via semi-rational design. It exhibited much improved catalytic efficiency towards (5*R*)-**1**. The K_m values of M3 for NADPH and (5*R*)-**1** were 0.15 mmol/L and 1.41 mmol/L, and the maximal reaction rate v_{max} was 55.56 μmol/min/mg. Compared with M1, the catalytic efficiency k_{cat}/K_m of M3 was increased 2.64-fold. Coupled with *Exiguobacterium sibiricum* glucose dehydrogenase (*Es*GDH) for nicotinamide adenine dinucleotide phosphate (NADPH) regeneration, M3 took 3.5 h to completely reduce (5*R*)-**1** at up to 100.0 g/L, producing 237.4 mmol/L (3*R*,5*R*)-**2** in *d.e.*$_p$ value above 99.5%. The space-time yield (STY) of M3-catalyzed (3*R*,5*R*)-**2** synthesis was 372.8 g/L/d.

1. Introduction

Atorvastatin, firstly marketed as a calcium salt under the brand name Lipitor®, possesses outstanding lipid-lowering efficacy, safety and long-term clinical benefits in reducing cardiovascular and cerebrovascular disease accidence and mortality [1,2]. So far, atorvastatin has cumulative sales exceeding 100 billion dollars, being the most successful drug in the history of the pharmaceutical industry [3].

t-Butyl 6-cyano-(3*R*,5*R*)-dihydroxyhexanoate ((3*R*,5*R*)-**2**) is the key bichiral diol intermediate of atorvastatin [4,5], therefore, studying the synthetic method of optically pure (3*R*,5*R*)-**2** is of great significance [3,6]. The synthetic methods documented mainly include borane-catalyzed reduction of *t*-butyl 6-cyano-(5*R*)-hydroxy-3-oxohexanoate ((5*R*)-**1**) and bio-asymmetric reductase (5*R*)-**1** to (3*R*,5*R*)-**2**. Borane-catalyzed reduction suffers from high energy consumption, low conversion rate, high production cost, etc [7]. As enzymes are the most proficient catalysts [8], bio-reduction has a lot of advantages over the chemical reduction, such as high stereoselectivity, few by-products, mild reaction conditions, and environmental friendliness [7,9].

Semi-rational design utilizes information on protein sequence, structure and function, as well as computational predictive algorithms to preselect promising target sites and limited amino acid diversity for protein engineering [10,11]. In recent years, the methodological advances in semi-rational design provide researchers with powerful and effective strategies to manipulate biocatalysts [10]. It has been used to raise fatty acid ω-hydroxylase activity [12], thermostability of nitrile hydratase [13], and alter selectivity of lipase [14], transglucosylase [15], nitrile hydratase [16], glycosyltransferase [17]. We constructed a variant of *Kluyveromyces lactis* aldo-keto reductase (*Kl*AKR) *Kl*AKR-Y295W/W296L that possessed improved catalytic efficiency towards (5*R*)-**1** by using a semi-rational design [18].

Previously, a novel M0 was cloned from a thermotolerant yeast *Kluyveromyces marxianus* ZJB14056, and its variant M1 was constructed, which retained good thermal stability and displayed moderate activity towards (5*R*)-**1** [19]. In this work, further semi-rational engineering of M1 was performed, and a new variant M3 was obtained with robust catalytic efficiency.

* Corresponding author at: College of Biotechnology and Bioengineering, Zhejiang University of Technology, Hangzhou, Zhejiang 310014, PR China.
E-mail address: wangyj@zjut.edu.cn (Y.-J. Wang).
[1] Both authors contributed equally to this work.

https://doi.org/10.1016/j.bioorg.2019.103018
Received 12 December 2018; Received in revised form 25 May 2019; Accepted 28 May 2019
Available online 08 June 2019

2. Materials and methods

2.1. Materials

2.1.1. Enzymes and reagents

Optically pure (5*R*)-**1** was generously presented by Zhejiang Lepu Pharmaceutical Co., Ltd (Taizhou, China). (3*R*,5*R*)-**2** was purchased from Toronto Research Chemicals Co., Ltd. (Toronto, Canada), NADPH from Roche Co., Ltd. (Basel, Switzerland), the restriction enzyme Dpn I from ThermoFisher Scientific Co., Ltd (Beijing, China), Phanta Super-Fidelity DNA polymerase from Vazyme Biotech Co., Ltd (Nanjing, China). The plasmid miniprep kit, DNA gel extraction kit and PCR cleanup kit were supplied by AxyPrep (Suzhou, China). Tryptone and yeast extract were acquired from Oxoid Corporation, kanamycin from Solarbio Science & Scientific Co., Ltd. (Beijing, China), isopropyl *β*-D-1-thiogalactopyranoside (IPTG) from Heli Biotechnology Co., Ltd (Shanghai, China). Unless otherwise specified, all other reagents and chemicals used in this study were obtained from local commercial suppliers, and used without further purification.

2.1.2. Bacteria, plasmids and culture media

Escherichia coli BL21(DE3) used for cloning and recombinant protein expression was purchased from Novagen (Shanghai, China). The *E. coli* BL21(DE3)/pET28b(+)-*esgdh* and *E. coli* BL21(DE3)/pET28a(+)-*kmakr*-W297H were constructed in our previous work, and deposited in our laboratory [19]. Primers synthesis and DNA sequencing were conducted at Tsingke Zixi Biotechnology Co., Ltd (Hangzhou, China).

Luria-Bertani (LB) medium consists of 10.0 g/L tryptone, 5.0 g/L yeast extract and 10.0 g/L NaCl, and was adjusted to pH 7.0 prior to sterilization. For slant preparation, LB medium was supplemented with 2.0% (*w/v*) agar.

2.2. Methods

2.2.1. Homology modeling and docking

M0 has a sequence identity of 49% to the conjugated polyketone reductase C1 from *Candida parapsilosis* IFO 0708 (CPR-C1, GenBank accession No.: BAD01652.1, PDB ID: 3WG6), which is the highest level among the structures that have been elucidated, hence the crystal structure of CPR-C1 was chosen as the template for *Km*AKR model-constructing [20]. The program Modeller 9.19 was used to model the three-dimension (3-D) structures of M0 and its variants. The constructed models were validated by the online software PROCHECK program, and molecular docking of (5*R*)-**1** into the "best" homology models was conducted with AutoDock 4.2 [21]. The 3-D structures of (5*R*)-**1** and NADPH were built with ChemDraw. All the modeling and molecular docking were visualized in the PyMOL.

2.2.2. Site-saturation mutagenesis (SSM)

A two-round of SSM at positions Tyr296 and Lys29 was conducted to investigate the *Km*AKR variants activities, in which the degenerate codon NNS was substituted for the codon of the target amino acids. In the first round of SSM, Tyr296 was subjected to saturation mutagenesis with pET28a(+)-*kmakr*-W297H as the template, accompanied by screening for the positive variants with enhanced catalytic efficiency. The pairwise primers were designed as follows: Tyr296-F: 5′-GTTAG-ATTGNNSTGGGTTGATTTCTACACCAAGTA-3′, Tyr296-R: 5′-ATCAAC-CCANNSCAATCTAACAGGTTCATGTTGTA −3′. The second round of SSM was performed at Lys29 using the "best" mutant pET28a(+)-*kmakr*-W297H/Y296W obtained from the first round of SSM on Tyr296 as the template, and pairwise primers designed as follows: Lys29-F: 5'-TGGTACNNSGCTGAAGAAACC-3', Lys29-R: 5'-TTCAGCN-NSGTACCACTTGGT-3'. The PCR reaction system (50 μL) consisted of 1 μL forward primer (100 μmol/L), 1 μL reverse primer (100 μmol/L), 25 μL 2 × Phanta Buffer, 1 μL dNTP mixture (each 10 mmol/L), 1 μL plasmid template, 1 μL DNA Polymerase, and 21 μL ultra-pure water. The PCR program was set according to the supplier's manual of Phanta Super-Fidelity DNA Polymerase as follows: 95 °C for 5 min, and then 29 cycles (95 °C for 15 s, 55 °C for 15 s, 72 °C for 7 min), followed by 72 °C extension for 10 min, 16 °C for insulation. The PCR products were digested by Dpn I at 37 °C for 3 h. The resultant recombinant plasmids were transferred into *E. coli* BL21(DE3) competent cells, and the clones were cultivated at 37 °C for 12 h. Then the positive clones were picked out and sterilely transferred into 10 mL of LB liquid medium supplemented with 50 μg/mL kanamycin, and cultivated at 37 °C, 180 rpm for 10 h. The positive clones were verified by DNA sequencing, then each broth was mixed with equal volume of sterilized 30% (*v/v*) glycerol aqueous solution, and deposited in a −80 °C refrigerator.

2.2.3. Cultivation

For preculture preparation, a single colony was picked up and sterilely transferred into 10 mL of LB liquid medium supplemented with 50 μg/mL kanamycin, and cultivated at 37 °C, 180 rpm for 10 h. 2 mL of preculture was transferred into 100 mL of LB liquid medium containing 50 μg/mL kanamycin, and incubated at 37 °C, 180 rpm till OD_{600} reached 0.6–0.8, at which point 0.15 mmol/L IPTG was added to induce *Km*AKRs expression. Induction cultivation was conducted at 28 °C, 180 rpm for 12 h.

The assay of screening reaction was conducted at 20.0 g/L (5*R*)-**1**, 30.0 g/L glucose, and cell lysates from 20.0 g/L *Km*AKR-harboring *E. coli* and 5.0 g/L GDH-harboring *E. coli*, 35 °C, pH 7.0 for 30 min.

2.2.4. Protein purification

M1 and its variants were purified as follows. Cells were harvested from the broth by centrifugation at 8000 rpm, 4 °C for 10 min, and washed twice with 0.9% (*w/v*) saline. The harvested wet cells were re-suspended in 100 mmol/L sodium phosphate buffer (pH 7.0) at 50 g/L, and the mixture was sonicated for 6 min (power 400 W, work for 1 s and break for 1 s). The supernatant of lysate was collected by centrifugation at 8000 rpm, 4 °C for 10 min, which was microfiltered through 0.45 μm membrane. The resultant filtrate was loaded on the Ni^{2+}-nitrilotriacetic acid column (Bio-Rad, USA), which was pre-equilibrated with buffer A (pH 8.0, 20 mmol/L sodium phosphate buffer, supplemented with 300 mmol/L NaCl and 20 mmol/L imidazole). Unbound impurities were washed out with buffer A at a flow rate of 1.0 mL/min until the conductivity became stable. Then target protein was eluted with buffer B (pH 8.0, 20 mmol/L sodium phosphate buffer supplemented with 300 mmol/L NaCl and 500 mmol/L imidazole). The collected eluate was dialyzed against 20 mmol/L phosphate buffer (pH 7.0) overnight. All purification steps were conducted at 4 °C. Proteins were identified with sodium dodecyl sulfate-polyacrylamide gel electrophoresis (SDS-PAGE).

2.2.5. Enzyme activity and kinetic parameters determination

The activity was tested under the standard conditions, which were 35 °C, 500 rpm, reaction time of 5 min, in a 1 mL reaction mixture composed of 100 mmol/L sodium phosphate buffer (pH 7.0) supplemented with 2.0 mmol/L (5*R*)-**1**, 0.25 mmol/L NADPH and 0.1 mg/mL purified *Km*AKRs. Each sample of 500 μL was periodically withdrawn, mixed with equal volume of anhydrous ethanol, and the resultant mixture was centrifuged at 12,000 rpm for 3 min. The supernatant was combined, and subjected to microfiltration with 0.22 μm membranes. The resulting filtrate was subsequently analyzed by High Performance Liquid Chromatography (HPLC).

For kinetic parameter measurements, the purified *Km*AKRs were used, and reactions were conducted at 35 °C, pH 7.0 for 3 min, with (5*R*)-**1** and NADPH concentrations of 2.0–10.0 mmol/L, 0.25–1.0 mmol/L, and 0.10 mg/mL purified *Km*AKRs, respectively. Since members of the AKR superfamily always follow the ordered *bi-bi* mechanism [22,23], values of Michaelis-Menten constant K_m and the maximal reaction rate v_{max} were regressed through nonlinear fitting of

the initial reaction rate Eq. (1)

$$v = \frac{v_{max}[A][B]}{K_m^A[B] + K_m^B[A] + K_S^A K_m^B + [A][B]} \quad (1)$$

where [A] is the concentration of NADPH, [B] is the concentration of (5*R*)-**1**, K_m^A, K_m^B represent Michaelis-Menten constants for NADPH and (5*R*)-**1**, and K_s^A is the dissociation constant of the enzyme-NADPH complex.

2.3. Enzymatic properties of M1 and its variants

2.3.1. Effect of temperature and pH

To investigate the temperature effect of on the activities of M1 and M3, their activities were measured in pH 7.0 phosphate buffer at temperatures ranging from 25 to 55 °C. For pH effect evaluation, their activities were tested at 35 °C, in 100 mmol/L acetate buffer of pH 5.0–6.0, 100 mmol/L sodium phosphate buffer of pH 6.0–8.0 and 100 mmol/L Tris-HCl buffer of pH 8.0–9.0. The reaction mixture composition, analytical methods were described in the Section 2.2.5.

2.3.2. Thermal stability

M1 and M3 were incubated at 40 °C, 50 °C for 15 h and 8 h, and samples were withdrawn at 1 h interval for the residual activity assay with the original activity defined as 100% [24]. Residual activity *y* decay with incubation time *t* was plotted with *y* on the ordinate and *t* on the abscissa, which was regressed with the nonlinear equation $y = A \cdot e^{-\frac{t}{t_1}} + y_0$ using Origin 9.1. Half-life, represented as $t_{1/2}$ is defined as the amount of time required for the residual activity of *Km*AKRs fall to 50%.

Circular dichroism (CD) analysis for M1 and M3 was conducted on Chirascan circular dichroism (CD) spectrometer (Applied Photophysics Ltd, United Kingdom). Enzyme samples were diluted with 20 mmol/L sodium phosphate buffer (pH 7.0) at a final protein concentration of 0.1 mg/mL, and then loaded to a 10 mm quartz cuvette for CD assay. The melting curve of *Km*AKRs were collected within the far-ultraviolet (180–260 nm) spectrum at temperatures of from 10 to 90 °C continuously. Data measured at wavelength of 222 nm were converted to fraction folded α according to Eq. (2),

$$\alpha = \frac{\theta_t - \theta_U}{\theta_F - \theta_U} \quad (2)$$

where θ_t is the observed ellipticity at any temperature, θ_F is the ellipticity of the fully folded form and θ_U is the ellipticity of the unfolded form [25,26]. The melting temperature (T_m) values were calculated from the CD using Origin 9.1 software.

2.3.3. Effect of metal ions and EDTA

To evaluate impacts of metal ions and chelating agent ethylenediaminetetraacetic acid (EDTA) on the activity of M1 and M3, the purified enzymes were incubated at 35 °C for 1 h with 1 mmol/L of EDTA, Fe^{3+}, Al^{3+}, Zn^{2+}, Fe^{2+}, Mg^{2+}, Co^{2+}, Ba^{2+}, Mn^{2+}, Ca^{2+}, Cu^{2+}, Ni^{2+} and Li^{+}, which were prepared with the corresponding concentrations of $Fe_2(SO_4)_3$, $Al_2(SO_4)_3$, $ZnSO_4$, $FeSO_4$, $MgSO_4$, $CoCl_2$, $BaCl_2$, $MnSO_4$, $CaCl_2$, $CuSO_4$, $NiCl_2$, CH_3COOLi. *Km*AKRs activities were determined under the standard conditions, denoted as the relative activities based on the original activity prior to incubation with the test metal ions and EDTA, which was designated as 100%.

2.4. Asymmetric reduction of (5R)-*1*

16.0 g DCW (dry cell weight)/L of each *E. coli* BL21(DE3)/pET28a(+)-*kmakr*-W297H/Y296W, *E. coli* BL21(DE3)/pET28a(+)-*kmakr*-W297H/Y296W/K29H mixed with 4.0 g DCW/L of *E. coli* BL21(DE3)/pET28b(+)-*esgdh* was suspended in pH 7.0, 100 mmol/L sodium phosphate buffer. Reactions were performed in 100-mL round bottom flasks, consisting of a certain amount of (5*R*)-**1** and 1.5-fold mass of glucose. Reaction temperature was controlled at 30 °C, rotation speed at 400 rpm (Scheme 1), and the pH of the reaction mixture was maintained at pH 7.0 with 1.0 mol/L Na_2CO_3 by using a pH-stat (Mettler Toledo, Switzerland). Each sample of 100 μL was periodically withdrawn, quenched by 900 μL anhydrous ethanol, and then subjected to HPLC analysis.

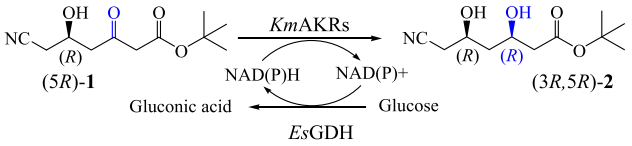

Scheme 1. Asymmetric reduction of (5*R*)-1 by *Km*AKRs coupled with *Es*GDH.

2.5. Analytical methods

(5*R*)-**1**, (3*R*,5*R*)-**2** and (3*S*,5*R*)-**2** were assayed with HPLC LC-10A system (Shimadzu, Japan) equipped with an ultraviolet detector SPD-10A VP Plus (Shimadzu, Japan) plus an ODS HYPERSIL column (4.6 × 250 mm, 5 μm, Thermo Scientific, USA). Column temperature was controlled at 40 °C. Mobile phase consists of acetonitrile and water at a volumetric ratio of 1:3 (*v*/*v*), and run at a flow rate of 1.0 mL/min, detector wavelength was set at 210 nm [19,27]. Enzymatic activity, specific activity, (5*R*)-**1** conversion, (3*R*,5*R*)-**2** yield and diastereomeric excess (*d.e.*$_P$) value were calculated based on the HPLC reports. All measurements were conducted in triplicate.

One unit (U) of enzyme activity was determined as the amount of the enzyme catalyzing the formation of 1 μmol of (3*R*,5*R*)-**2** per minute at 35 °C, pH 7.0. Specific activity was calculated as the units of enzyme activity per milligram of proteins, U/mg protein. For DCW measurement, cells were first pelleted by centrifuging at 13200*g*, 4 °C for 10 min, and then dried at 80 °C to a constant weight in a drying oven.

3. Results and discussion

3.1. Homology modeling and docking

At present, no crystal structures of *Km*AKR are available; therefore, molecular modeling and homology model construction represent the most accessible approaches to understand and visualize their conformations and substrate binding for the case of M0 and other variants. In this study, a homology model of the M0 was constructed using the CPR-C1 (GenBank accession No.: BAD01652.1, PDB ID: 3WG6) as the construction template since its crystal structure has been elucidated and they share 49% sequence identity (Fig. S1). The refined 3-D structure of M0 was validated by PROCHECK program, with 90.7% amino acids in the most reasonable area, 6.8% amino acids in the extra reasonable area, 1.4% amino acids in the generally reasonable area and 1.1% amino acids in the unreasonable area, suggesting the constructed 3-D model is reasonably credible (Fig. S2a). As depicted in Fig. S2b, M0 has the typical $(\alpha/\beta)_8$ barrel structure (TIM structure), which is the conserved structure of the AKR superfamily [28,29]. Moreover, M0 has a catalytic tetrad of Asp59-Tyr64-Lys89-His122, located in the active center [20,30].

Molecular docking of (5*R*)-**1** into M1 showed that the distance between the H atom of Tyr64-OH and the carbonyl oxygen atom of (5*R*)-**1** is 3.30 Å, the distance is close to the hydrogen bond distance (3.4 Å) between the carboxylate of substrate and residue Tyr48 of ALR2 (an aldose reductase) [31], and consistent with hydrogen bonding interactions based on a commonly accepted criteria, *i. e.* the distance between the hydrogen bond donor and the acceptor atoms is less than 3.5 Å [32]. The distance of the H atom at C4 of NADPH to the carbonyl carbon of (5*R*)-**1** is 3.11 Å, which is close to the distance between acceptor carbonyl group and C4 atom of $NADP^+$ (3.2 Å), reported by

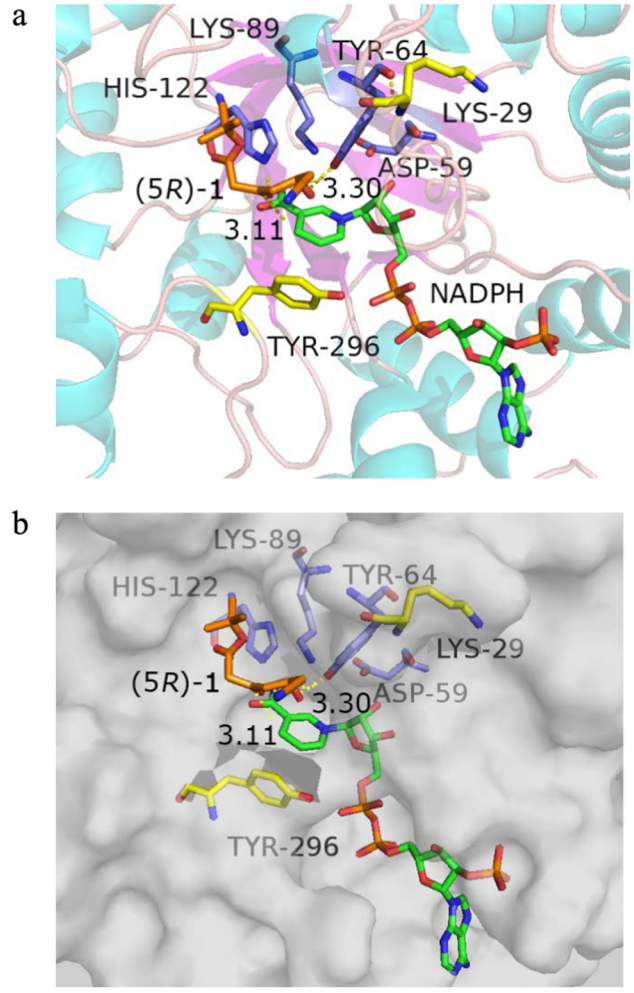

Fig. 1. Molecular docking of NADPH and (5*R*)-1 into M1 (a), and view of the surface of M1 with NADPH and (5*R*)-1 molecule (ball-and-stick) bound in the active site (b). (5*R*)-1 and NADPH are highlighted in orange and green respectively, the mutant sites (296, 29) and the catalytic tetrad (Asp59-Tyr64-Lys89-His122) in yellow and blue. The dockings of substrates were conducted with AutoDock 4.2. Pictures were drawn with PyMOL. (For interpretation of the references to colour in this figure legend, the reader is referred to the web version of this article.)

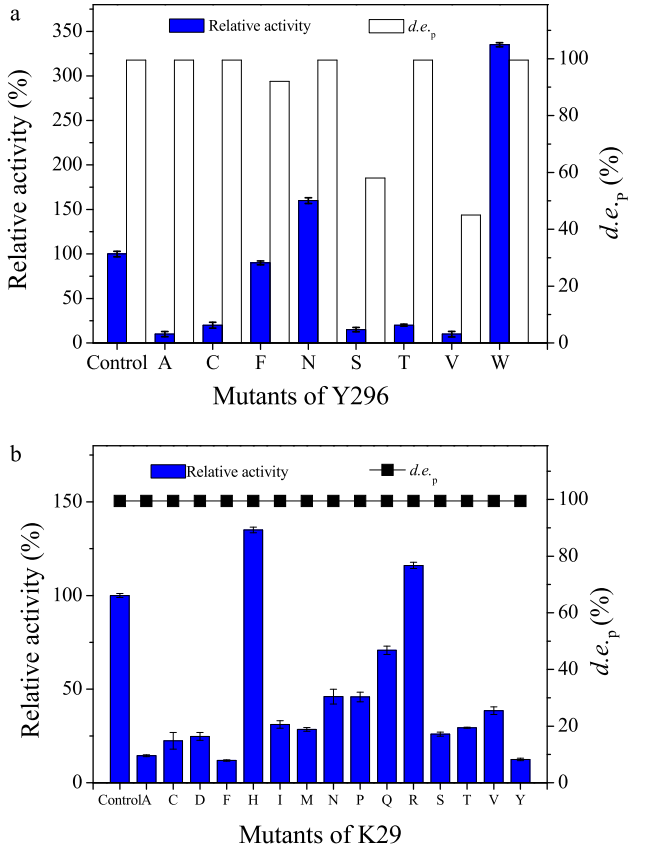

Fig. 2. Effect of mutations at Y296 and K29 on the relative activity and stereoselectivity of *Km*AKR towards (5*R*)-1. (a), control is M1, whose activity is designated as 100%. (b), control is M2, whose activity is designated as 100%. Activity was measured under the standard assay conditions. The values are the means of three individual experiments.

Zheng et al. [33]. Taken together, the docked *Km*AKR-NADPH-(5*R*)-**1** complex structure is reasonable, which can be used for precise description of the substrate-binding site and the putative interactions, and indicates the conformation is catalytically competent (Fig. 1a). Therefore, the docking is reasonable.

Apart from spatial distance, side chain's size and charge of the residues spatially adjacent to the active center affects catalytic efficiency [34,35]. As shown in Fig. 1b, Tyr296 and Lys29 are close to the active center, and Tyr296 is non-polar, uncharged amino acid and participates in hydrophobic interactions with other amino acids as well as (5*R*)-**1**. It is reasonable to further enhance the binding force via replacing Tyr296 with other amino acids with stronger hydrophobicity. Meanwhile, Tyr64 is the catalytic residue and proton donor, and forms a hydrogen bond with Lys29, whose role in enzyme conformation deserves deep investigation. Therefore, Tyr296 and Lys29 were chosen for the following SSM study.

3.2. SSM study on M1

SSM provides a rapid and simple method to generate novel protein variants [36,37]. In present work, two target residues Tyr296 and Lys29 were subjected to SSM and screened. The first round of SSM library screening on Tyr296 produced the fittest candidate W297H/Y296W, resulting in a 2.35-fold increment in activity with excellent selectivity ($d.e._P$ > 99.5%) remained (Fig. 2a). An explanation is that Trp is nonpolar, more hydrophobic, contributing to stronger affinity to (5*R*)-**1**.

The second-round of SSM experiment on Lys29 was conducted with *Km*AKR-W297H/Y296W (M2) as the template. The SSM library screening on Lys29 yielded positive variants M3 and W297H/Y296W/K29R, showing 0.35, 0.16-fold increase in the value of activity (Fig. 2b). Lys, Arg and His are positively charged basic amino acids, and the side chain of His is a sterically hindered imidazole group. It was suggested that positively charged basic amino acids with large steric hindrance are favorite at position 29 for improving activity. As shown in Fig. S3, the majority of M1 and its variants M2, M3 were expressed in the soluble form, with a small amount of inclusion bodies formed. The purified proteins appeared as a single band corresponding to a molecular size of approximately 36 kDa, consistent with that of M0 [19]. As expected, there were no obvious differences in protein expression levels between M1, M2 and M3.

3.3. Enzymatic properties of M1 and its variants

3.3.1. Effects of temperature and pH

Temperature and pH play vital roles in enzyme activity and stability. The optimal temperature of M0 was 35 °C [19]. As shown in Fig. S4, the activities of both M1 and M3 approached a plateau at 35 °C, peaking at 3.77 U/mg and 5.47 U/mg, respectively. Mutations on Trp297, Tyr296 and Lys29 did not change *Km*AKR's temperature optimum.

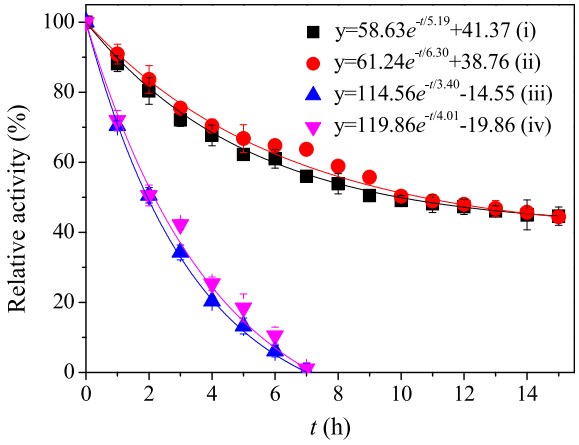

Fig. 3. Effect of temperature on the activities of M1 and M3. Equations *i*, *iii* correspond to the relationships between the residual activities of M1 at 40 °C and 50 °C and incubation time. Equations *ii*, *iv* correspond to the relationships between the residual activities of M3 at 40 °C and 50 °C and incubation time.

M0′s optimum pH value was 7.0 [19]. Also, M1 and M3 were most active at pH 7.0, peaking at 3.77 U/mg and 5.56 U/mg, respectively (Fig. S5). Similar to optimum temperature, mutations on Trp297, Tyr296 and Lys29 did not alter M0's optimum pH.

3.3.2. Thermal stability

As presented in Fig. 3, when temperature was elevated to 50 °C, a marked reduction in activity was observed. The $t_{1/2}$ and k_d data of M1 and M3 at 40 °C and 50 °C were tabulated in Table 1. The half-lives $t_{1/2}$ of M1 at 40 °C and 50 °C were 596.4 min and 117.0 min, respectively; $t_{1/2}$ of M3 at 40 °C, 50 °C was 639.6 min, 130.2 min.

T_m for thermostability assessment was also characterized. As the temperature increased, the negative peak intensity of M1 and M3 at 222 nm gradually decreased (Fig. S6). As tabulated in Table 2, the T_m value of M3 was 61.2 °C, which is 3.7 °C higher than that of M1 (57.5 °C). The triple mutation M3 caused a slightly improvement in the enzyme's thermostability.

3.3.3. Kinetic parameter and catalytic efficiency

As tabulated in Table 2, the K_m values of M2 for NADPH and the substrate (5*R*)-**1** were 0.15 mmol/L and 1.42 mmol/L; for M3, the K_m values were 0.15 mmol/L and 1.41 mmol/L, and the maximum reaction rates v_{max} were 49.50 μmol/min/mg and 55.56 μmol/min/mg, respectively. The catalytic efficiencies of M3, M2 were 2.64, 2.20-fold higher than that of parental M1, the catalytic efficiencies of M3, M2 and M1 were 14.56, 16.69, 3.86 times higher than that of M0 [19].

3.3.4. Effects of metal ions and EDTA

Effects of metal ions and EDTA on M1 and M3 activities were presented in Table 3. No significantly improvement in activity was observed by metal ions addition, and 1.0 mmol/L of Fe^{3+}, Al^{3+}, Zn^{2+}, Co^{2+}, Cu^{2+} and Ni^{2+} had inhibitory effects on activity to varying degrees.

Table 1
Thermal stability of M1 and M3.

Variant	k_d (1/h)[a]	$t_{1/2}$ (min)[b]	k_d (1/h)[a]	$t_{1/2}$ (min)[b]	T_m (°C)
	40 °C		50 °C		
M1	0.070	596.4	0.355	117.0	57.5
M3	0.065	639.6	0.319	130.2	61.2

T_m: melting temperature.
[a] k_d: inactivation rate constant.
[b] $t_{1/2}$: the half-life of the enzymes, at which the residual enzyme activity is the half of the initial enzyme activity at a certain temperature.

Table 2
Kinetic parameters of *Km*AKR and its variants towards (5*R*)-1.

Enzyme	v_{max} (μmol/min/mg)	k_{cat}[a] (1/s)	$K_{m,A}$ (mmol/L)	$K_{m,B}$ (mmol/L)	$(k_{cat}/K_m)_A$ (L/mmol/s)	$(k_{cat}/K_m)_B$ (L/mmol/s)
M0	4.48	2.72	0.18	2.01	15.11	1.35
M1	17.09	10.36	0.17	1.58	60.94	6.56
M2	49.50	29.84	0.15	1.42	198.93	21.01
M3	55.56	33.67	0.15	1.41	224.47	23.88

[a] Turnover number $k_{cat} = v_{max}/[E]$, where [E] is the molar concentration of enzymes.

Table 3
Effects of metal ions and EDTA on the activities of M1 and M3.

Metal ion	Concentration (mmol/L)	Relative activity (%)	
		M1	M3
Control	/	100	100
Fe^{3+}	1.0	84 ± 1.83	88 ± 0.63
Al^{3+}	1.0	88 ± 0.73	101 ± 1.52
Zn^{2+}	1.0	86 ± 0.97	68 ± 2.63
Fe^{2+}	1.0	90 ± 2.31	93 ± 0.83
Mg^{2+}	1.0	88 ± 1.52	99 ± 0.52
Co^{2+}	1.0	87 ± 0.36	85 ± 0.83
Ba^{2+}	1.0	84 ± 1.26	105 ± 1.28
Mn^{2+}	1.0	95 ± 0.85	96 ± 0.26
Ca^{2+}	1.0	83 ± 0.54	105 ± 1.85
Cu^{2+}	1.0	88 ± 1.24	78 ± 0.69
Ni^{2+}	1.0	89 ± 0.92	65 ± 0.39
Li^{+}	1.0	112 ± 0.73	98 ± 2.05
EDTA	1.0	91 ± 0.75	96 ± 1.25

Activity was measured under the standard assay conditions after M1 and M3 exposure to various metal ions and chemical agents at 35 °C for 1 h. The activity of M1 and M3 detected in the absence of the test metal ions and EDTA was recorded as 100%. All reactions were performed in triplicate, and all activities were expressed as means ± standard deviations.

3.4. Mechanic analysis of strict stereoselectivity and enhancement of enzymatic activity

The reaction mechanism of NAD(P)H-dependent dehydrogenase has been studied in detail [38]. The mechanism of NADPH-dependent bioreductions involves a hydride transfer from NADPH to carbonyl carbon and a proton transfer from the catalytic residue to carbonyl oxygen [39]. Upon formation of the *Km*AKR-NADPH-(5*R*)-**1** ternary complex, a hydride is transferred from the C4 carbon atom of the nicotinamide ring (4′-*pro*-*R* hydrogen) of NADPH to the carbonyl carbon of the substrate while a proton is provided by the protonated catalytic residue Tyr64 to the carbonyl oxygen. Totally, there are four different manners of 4′-*pro*-*R* hydrogen and 4′-*pro*-*S* hydrogen at C4 of NADPH attacking the carbonyl carbon of (5*R*)-**1**, forming two different configurations of chiral alcohol [40]. As shown in Fig. 4b and 4c, the docking results indicated the 4′-*pro*-*R* and 4′-*pro*-*S* hydrides could attack from the *si* face of (5*R*)-**1**, producing (3*R*,5*R*)-**2**, following the *anti*-Prelog's rule; also, they can attack the *re* face of (5*R*)-**1** to form (3*S*,5*R*)-**2** [41]. According to our experimental results, the product was (3*R*,5*R*)-**2**, indicating that M2 and M3 follows the *anti*-Prelog' rule.

Docking NADPH and (5*R*)-**1** into the active sites of M1 and its variants was performed to elucidate the mechanism of activity enhancement brought by mutations on Trp297, Tyr296 and Lys29. For M2, hydrogen bonds were formed between the carbonyl of (5*R*)-**1** in both orientations and the side chains of Tyr64 and His122 (Fig. 4a and d), indicating docking results are meaningful. Substituting Tyr296 with

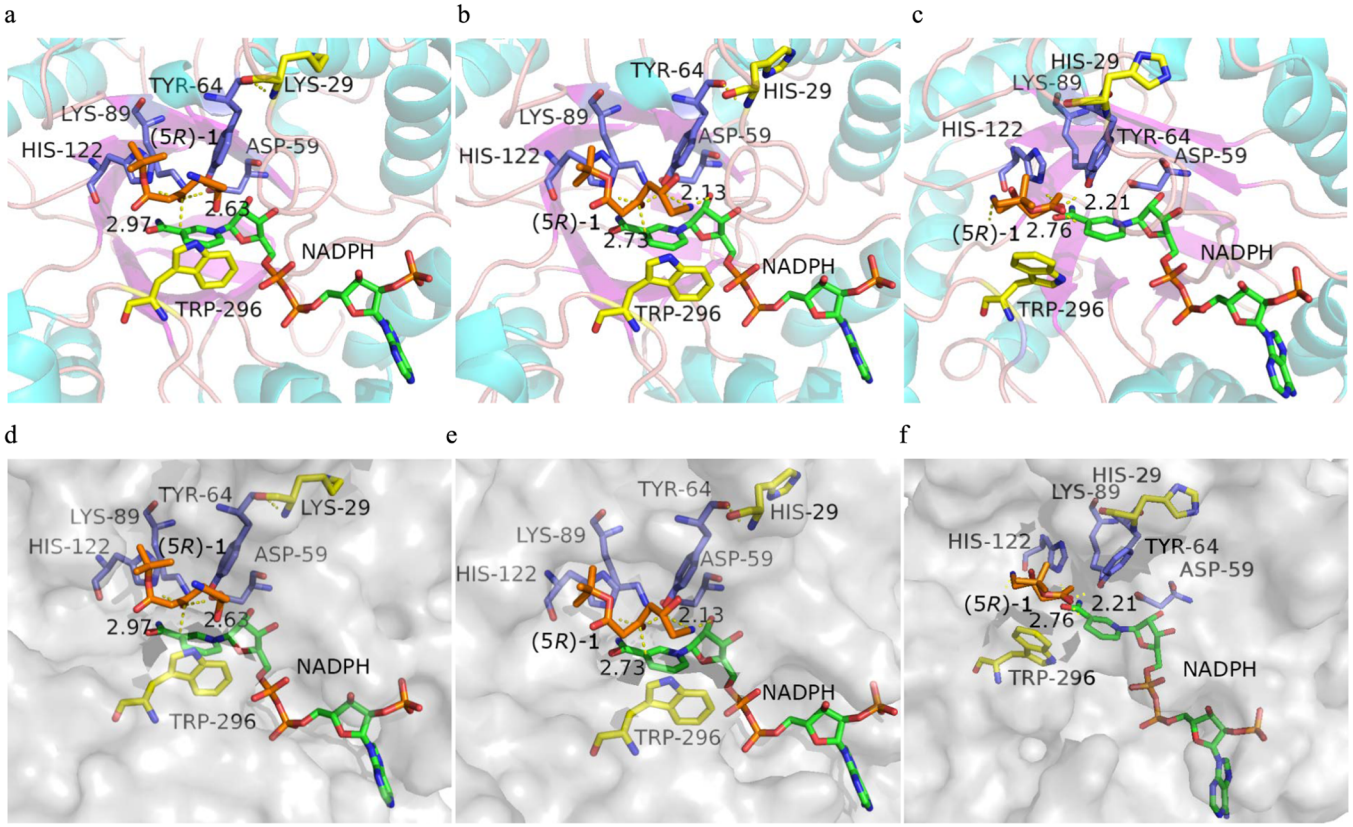

Fig. 4. Molecular docking of NADPH and (5*R*)-1 into M2 (a) and M3 (b, c), and views of the surface of M2 (d), M3 (e, f) with NADPH and (5*R*)-1 molecule (ball-and-stick) bound in the active site. The *si* face of (5*R*)-1 faces the catalytic site (b); the *re* face of (5*R*)-1 faces the catalytic site (c); the *si* face of (5*R*)-1 faces the catalytic site (e); the *re* face of (5*R*)-1 faces the catalytic site (f). (5*R*)-1 and NADPH are shown in orange and green, the mutant sites (296, 29) and the catalytic tetrad (Asp59-Tyr64-Lys89-His122) are shown in yellow and blue, respectively. The dockings of substrate were conducted with AutoDock 4.2. Pictures were drawn with PyMOL. (For interpretation of the references to colour in this figure legend, the reader is referred to the web version of this article.)

Trp shortened the distance between the proton of catalytic residue Tyr64-OH and the carbonyl oxygen of (5*R*)-**1** from 3.30 Å to 2.63 Å. The distance of the 4′-*pro-R* hydrogen of NADPH to the carbonyl carbon of (5*R*)-**1** was shortened from 3.11 Å to 2.97 Å (Figs. 1a and 4a). These shortenings made the enzyme catalytic center network more compact, attributing to enhanced transfer rates of hydrides and protons.

As shown in Fig. 4b, mutation of K29H further shorten the distance between the proton of the catalytic residue Tyr64-OH and the carbonyl oxygen of (5*R*)-**1** to 2.13 Å, compared to M2. The carbonyl carbon of (5*R*)-**1** is much closer to the 4′-*pro-R* hydrogen of NADPH with the distance reduced from 2.97 Å to 2.73 Å in the case of M2, satisfies the distance requirement for hydride transfer [42], which is more conducive to the attack of hydride to the carbonyl carbon. Mutating Tyr296 to the more hydrophobic Trp pushing (5*R*)-**1** more adjacent to the active center, linked with increasing hydrophobic interactions. Moreover, when the Lys29 was mutated to His, the active site tunnel broadened around the nicotinamide (Fig. 4d and e). The catalytic center was significantly enlarged compared to M1, facilitating (5*R*)-**1** binding and shuttling, facilitating substrate molecules contact with enzyme, which increases catalytic efficiency.

As for M3, viewed from the *si* face, the carbonyl carbon of (5*R*)-**1** is much closer to the 4′-*pro-R* hydride of NADPH than that of the *re* face. When the *si* face of (5*R*)-**1** faces the catalytic center, the substrate-binding pocket was further enlarged compared to the *re* face (Fig. 4e and f), facilitating (5*R*)-**1** binding and shuttling.

3.5. (3*R*,5*R*)-2 bioconversion kinetics

Due to the high cost of NADPH, an *Es*GDH-mediated NADPH regeneration system was introduced, which consumed inexpensive glucose as hydrogen donor, as shown in Fig. 5. Under the optimized conditions, M2 was able to completely reducing up to 75.0 g/L (5*R*)-**1** in 4.5 h to obtain (3*R*,5*R*)-**2**, in $d.e._P$ > 99.5%. M3 completely reduced 100 g/L (5*R*)-**1** within 3.5 h, producing 237.4 mmol/L of (3*R*,5*R*)-**2**, resulting in a STY of 372.8 g/L/d. Further raising (5*R*)-**1** to 120.0 g/L reduced substrate conversion to 93.8%, demonstrating that excessive (5*R*)-**1** loading brought about substrate inhibition on enzyme.

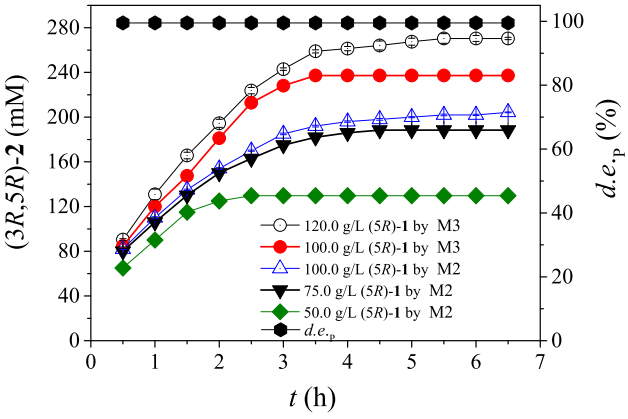

Fig. 5. Conversion profile of M2 and M3 catalyzed reduction of (5*R*)-1 to (3*R*,5*R*)-2.

To the best of our knowledge, rare AKRs and carbonyl reductases have been reported with strict stereoselectivity and high activity towards (5*R*)-**1**. As summarized in Table 4, *E. coli* BL21/pET28a-*Lb*CR has the highest substrate load, and requires 16 h of conversion time for

Table 4
Comparison of oxidoreductase-catalyzed asymmetric reduction of (5*R*)-**1** to (3*R*,5*R*)-**2**.

Enzyme	Microorganism source	Biocatalyst loading size (g DCW/L)	(5*R*)-**1** (g/L)	Conversion (%)	Conversion time (h)	STY (g/L/d)	$d.e._p$ (%)	Reference
CR1	*Saccharomyces cerevisiae*	8.2	35	> 99	7	120	> 99.5	[43]
*Kl*AKR-Y295W/W296L	*Kluyveromyces lactis*	20	50	> 99	1.3	623.6	> 99.5	[18]
*Lb*CR	*Lactobacillus brevis*	16	300	> 99	16	351	> 99.5	[44]
*Es*GDH-*Kl*AKR-Y295W/W296LW296L	*Kluyveromyces lactis*	20	60	100	4	243.2	99.5	[27]
M1	*Kluyveromyces marxianus*	20	38	> 99	12	45.4	> 99.5	[19]
M3	*Kluyveromyces marxianus*	20	100	> 99	3.5	372.8	> 99.5	Present work

complete conversion. *E. coli* BL21(DE3)/pET28a(+)-*kmakr*-W297H/Y296W/K29H has the highest substrate load among the AKRs, and the second highest STY, only ranking after *E. coli* BL21/pET28b-*klakr*-Y295W/W296L.

4. Conclusions

M1 has moderate activity towards (5*R*)-**1**. In this work, semi-rational design was used to further evolve M1. A "best" variant M3 with significantly enhanced catalytic performance was obtained through a two-round of SSM library screening. Replacing Tyr296 to Trp further consolidated the enzyme-substrate binding via pushing (5*R*)-**1** close to the active site. Mutating Lys29 to His enlarged the enzyme active pocket. Besides, mutations of Y296W and K29H shortened the distance between the H atom of catalytic site Tyr64-OH and the carbonyl oxygen atom of (5*R*)-**1**, accelerating the transfer rates of protons and electron. Coupled with *Es*GDH for NADPH regeneration, M3 was able to completely reduce 100.0 g/L (5*R*)-**1** in as short as 3.5 h, resulting in a high STY of 372.8 g/L/d. Thanks to its strict diastereoselectivity, good thermal stability and high activity, a promising platform technology based on the combination of stereoselective AKR and GDH is constructed, enabling efficiently converting prochiral ketones to optically pure secondary alcohols.

Acknowledgments

This work was financially supported by the Natural Science Foundation of China (21878274, 21476209) and the Major Program for Key Science and Technology of Zhejiang Province of China (2014C03010).

Appendix A. Supplementary material

Supplementary data to this article can be found online at https://doi.org/10.1016/j.bioorg.2019.103018.

References

[1] K.F. Croom, G.L. Plosker, Atorvastatin-a review of its use in the primary prevention of cardiovascular events in patients with type 2 diabetes mellitus, Drugs 65 (2005) 137–152.
[2] N. Andrushko, V. Andrushko, V. Tararov, A. Korostylev, G. König, A. Börner, Highly stereoselective hydrogenations-as key-steps in the total synthesis of statins, Chirality 22 (2010) 534–541.
[3] J.M. Patel, Biocatalytic synthesis of atorvastatin intermediates, J. Mol. Catal. B: Enzym. 61 (2009) 123–128.
[4] S. George, A. Sudalai, An efficient organocatalytic route to the atorvastatin side-chain, Tetrahedron Lett. 48 (2007) 8544–8546.
[5] X. Wu, L. Wang, S. Wang, Y. Chen, Stereoselective introduction of two chiral centers by a single diketoreductase: an efficient biocatalytic route for the synthesis of statin side chains, Amino Acids 39 (2010) 305–308.
[6] A. Liljeblad, A. Kallinen, L.T. Kanerva, ChemInform abstract: biocatalysis in the preparation of the statin side chain, Curr. Org. Synth. 6 (2015) 362–379.
[7] J.M. Woodley, New opportunities for biocatalysis: making pharmaceutical processes greener, Trends Biotechnol. 26 (2008) 321–327.
[8] J.M. Choi, S.S. Han, H.S. Kim, Industrial applications of enzyme biocatalysis: current status and future aspects, Biotechnol. Adv. 33 (2015) 1443–1454.
[9] P. Wei, J.X. Gao, G.W. Zheng, H. Wu, M.H. Zong, W.Y. Lou, Engineering of a novel carbonyl reductase with coenzyme regeneration in *E. coli* for efficient biosynthesis of enantiopure chiral alcohols, J. Biotechnol. 230 (2016) 54–62.
[10] S. Lutz, Beyond directed evolution-semi-rational protein engineering and design, Curr. Opin. Biotechnol. 21 (2010) 734–743.
[11] F. Cheng, X.L. Tang, T. Kardashliev, Transcription factor-based biosensors in high-throughput screening: advances and applications, Biotech. J. 13 (2018) 1700648.
[12] E. Jung, B.G. Park, H.W. Yoo, J. Kim, K.Y. Choi, B.G. Kim, Semi-rational engineering of CYP153A35 to enhance omega-hydroxylation activity toward palmitic acid, Appl. Microbiol. Biotechnol. 102 (2018) 269–277.
[13] Y.Y. Xia, W.J. Cui, Z.Y. Cheng, L. Peplowski, Z.M. Liu, M. Kobayashi, Z.M. Zhou, Improving the thermostability and catalytic efficiency of the subunit-fused nitrile hydratase by semi-rational engineering, ChemCatChem 10 (2018) 1370–1375.
[14] K. Zorn, I. Oroz-Guinea, H. Brundiek, M. Dorr, U.T. Bornscheuer, Alteration of chain length selectivity of *candida antarctica* lipase a by semi-rational design for the enrichment of erucic and gondoic fatty acids, Adv. Synth. Catal. 360 (2018) 4115–4131.

[15] T. Verhaeghe, K. De Winter, M. Berland, R. De Vreese, M. D'hooghe, B. Offmann, T. Desmet, Converting bulk sugars into prebiotics: semirational design of a transglucosylase with controlled selectivity, Chem. Commun. 52 (2016) 3687–3689.
[16] Z.Y. Cheng, L. Peplowski, W.J. Cui, Y.Y. Xia, Z.M. Liu, J.L. Zhang, M. Kobayashi, Z.M. Zhou, Identification of key residues modulating the stereoselectivity of nitrile hydratase toward *rac*-mandelonitrile by semi-rational engineering, Biotechnol. Bioeng. 115 (2018) 524–535.
[17] B. Fan, W.X. Dong, T.Y. Chen, J.L. Chu, B.F. He, Switching glycosyltransferase UGT(BL)1 regioselectivity toward polydatin synthesis using a semi-rational design, Org. Biomol. Chem. 16 (2018) 2464–2469.
[18] X. Luo, Y.J. Wang, W. Shen, Y.G. Zheng, Activity improvement of a *Kluyveromyces lactis* aldo-keto reductase *Kl*AKR via rational design, J. Biotechnol. 224 (2016) 20–26.
[19] Y.J. Wang, B.B. Ying, W. Shen, R.C. Zheng, Y.G. Zheng, Rational design of *Kluyveromyces marxianus* ZJB14056 aldo-keto reductase *Km*AKR to enhance diastereoselectivity and activity, Enzyme Microb. Technol. 107 (2017) 32–40.
[20] H.M. Qin, A. Yamamura, T. Miyakawa, M. Kataoka, T. Nagai, N. Kitamura, N. Urano, S. Maruoka, J. Ohtsuka, K. Nagata, Structure of conjugated polyketone reductase from *Candida parapsilosis* IFO 0708 reveals conformational changes for substrate recognition upon NADPH binding, Appl. Microbiol. Biotechnol. 98 (2014) 243–249.
[21] T. Oleg, A.J. Olson, Software news and update AutoDock Vina: improving the speed and accuracy of docking with a new scoring function, efficient optimization, and multithreading, J. Comput. Chem. 31 (2010) 455–461.
[22] S. Zuccotti, D. Zanardi, C. Rosano, L. Sturla, M. Tonetti, M. Bolognesi, Kinetic and crystallographic analyses support a sequential-ordered BiBi catalytic mechanism for *Escherichia coli* glucose-1-phosphate thymidylyltransferase, J. Mol. Biol. 313 (2001) 831–843.
[23] W.C. Cooper, Y. Jin, T.M. Penning, Elucidation of a complete kinetic mechanism for a mammalian hydroxysteroid dehydrogenase (HSD) and identification of all enzyme forms on the reaction coordinate-the example of rat liver 3 alpha-HSD (AKR1C9), J. Biol. Chem. 282 (2007) 33484–33493.
[24] J. Huang, D.F. Xie, Y. Feng, Engineering thermostable (*R*)-selective amine transaminase from *Aspergillus terreus* through in silico design employing B-factor and folding free energy calculations, Biochem. Biophys. Res. Commun. 483 (2017) 397–402.
[25] B. Benjamin, J.J. Havranek, Automated selection of stabilizing mutations in designed and natural proteins, Proc. Natl. Acad. Sci. USA 109 (2012) 1494–1499.
[26] N.J. Greenfield, Analysis of circular dichroism data, MethodsEnzymol. 383 (2004) 282–317.
[27] Y.J. Wang, W. Shen, X. Luo, Z.Q. Liu, Y.G. Zheng, Enhanced diastereoselective synthesis of *t*-butyl 6-cyano-(3*R*,5*R*)-dihydroxyhexanoate by using aldo-keto reductase and glucose dehydrogenase co-producing engineered *Escherichia coli*, Biotechnol. Progr. 33 (2017) 1235–1242.
[28] S.S. Hoog, J.E. Pawlowski, P.M. Alzari, T.M. Penning, M. Lewis, Three-dimensional structure of rat liver 3α-hydroxysteroid/dihydrodiol dehydrogenase: a member of the aldo-keto reductase superfamily, Proc. Natl. Acad. Sci. USA 91 (1994) 2517–2521.
[29] T.M. Penning, The aldo-keto reductases (AKRs): overview, Chem. Biol. Interact. 234 (2015) 236–246.
[30] J.M. Jez, M.J. Bennett, B.P. Schlegel, M. Lewis, T.M. Penning, Comparative anatomy of the aldo-keto reductase superfamily, Biochem. J. 326 (1997) 625–636.
[31] Z.G. Wang, S. Zhou, S.L. Zhang, S. Zhang, F.M. Zhu, X.L. Jin, Z.M. Chen, X.L. Xu, Semi-rational engineering of a thermostable aldo-keto reductase from *Thermotoga maritima* for synthesis of enantiopure ethyl-2-hydroxy-4-phenylbutyrate (EHPB), Sci. Rep. 7 (2017) 4007.
[32] X.H. Zheng, L.P. Zhang, W.J. Chen, Y.Y. Chen, W. Xie, X.P. Hu, Partial inhibition of aldose reductase by nitazoxanide and its molecular basis, ChemMedChem 7 (2012) 1921–1923.
[33] V. Carbone, M. Giglio, R. Chung, T. Huyton, J. Adams, R. Maccari, R. Ottana, A. Hara, O. El-Kabbani, Structure of aldehyde reductase in ternary complex with a 5-arylidene-2,4-thiazolidinedione aldose reductase inhibitor, Eur. J. Med. Chem. 45 (2010) 1140–1145.
[34] G.W. Zheng, J.H. Xu, New opportunities for biocatalysis: driving the synthesis of chiral chemicals, Curr. Opin. Biotechnol. 22 (2011) 784–792.
[35] Z.Q. Liu, W. Zheng, J.F. Huang, L.Q. Jin, D.X. Jia, H.Y. Zhou, J.M. Xu, C.J. Liao, X.P. Cheng, B.X. Mao, Improvement and characterization of a hyperthermophilic glucose isomerase from *Thermoanaerobacter ethanolicus* and its application in production of high fructose corn syrup, J. Ind. Microbiol. Biotechnol. 42 (2015) 1091–1103.
[36] R.M.P. Siloto, R.J. Weselake, Site saturation mutagenesis: methods and applications in protein engineering, Biocatal. Agric. Biotechnol. 1 (2012) 181–189.
[37] A. Li, C.G. Acevedo-Rocha, M.T. Reetz, Boosting the efficiency of site-saturation mutagenesis for a difficult-to-randomize gene by a two-step PCR strategy, Appl. Microbiol. Biotechnol. 102 (2018) 6095–6103.
[38] S. Kara, J.H. Schrittwieser, F. Hollmann, M.B. Ansorge-Schumacher, Recent trends and novel concepts in cofactor-dependent biotransformations, Appl. Microbiol. Biotechnol. 98 (2014) 1517–1529.
[39] A. Urzhumtsev, F. TeteFavier, A. Mitschler, J. Barbanton, P. Barth, L. Urzhumtseva, J.F. Biellmann, A.D. Podjarny, D. Moras, A 'specificity' pocket inferred from the crystal structures of the complexes of aldose reductase with the pharmaceutically important inhibitors tolrestat and sorbinil, Structure 5 (1997) 601–612.
[40] T. Matsuda, R. Yamanaka, K. Nakamura, Recent progress in biocatalysis for asymmetric oxidation and reduction, Cheminform 20 (2009) 513–557.
[41] M.M. Musa, R.S. Phillips, Recent advances in alcohol dehydrogenase-catalyzed asymmetric production of hydrophobic alcohols, Catal. Sci. Technol. 1 (2011) 1311–1323.
[42] P.K. Agarwal, S.P. Webb, S. Hammes-Schiffer, Computational studies of the mechanism for proton and hydride transfer in liver alcohol dehydrogenase, J. Amer. Chem. Soc. 122 (2000) 4803–4812.
[43] X. Wu, X. Gou, Y. Chen, Enzymatic preparation of *t*-butyl-6-cyano-(3*R*,5*R*)-dihydroxyhexanoate by a whole-cell biocatalyst co-expressing carbonyl reductase and glucose dehydrogenase, Process Biochem. 50 (2015) 104–110.
[44] X.M. Gong, G.W. Zheng, Y.Y. Liu, J.H. Xu, Identification of a robust carbonyl reductase for diastereoselectively building syn-3,5-dihydroxy hexanoate: a bulky side chain of atorvastatin, Org. Process Res. Dev. 21 (2017) 1349–1354.